SCIENTIFIC REPORTS

OPEN

Emission-wavelength-dependent photoluminescence decay lifetime of N-functionalized graphene quantum dot downconverters: Impact on conversion efficiency of Cu(In, Ga)Se$_2$ solar cells

Firoz Khan[1] & Jae Hyun Kim[2]

Graphene quantum dots (GQDs) have several advantages over inorganic quantum dots owing to their beneficial properties. Recently, GQDs have been used as downconverters in photovoltaic devices. However, the application of GQDs in most emergent thin-film-based Cu(In, Ga)Se$_2$ (CIGS) photovoltaic cells is limited because of either low photoluminescence (PL) quantum yield (QY) or a small Stokes shift ($\Delta\lambda$). Therefore, GQDs with an ultrahigh QY and large $\Delta\lambda$ are essential to realizing the two emergent fields, i.e., the application of GQDs in CIGS photovoltaic solar cells. In this regard, we synthesized nitrogen-functionalized GQDs (NGQDs) with an ultrahigh QY (77–99%) and a large $\Delta\lambda$ (95–155 nm) via tailoring of the nitrogen and oxygen moieties. The NGQDs were applied in CIGS solar cells to evaluate their downconversion efficiency. Our study shows that the emission wavelength (λ_{em})-dependent photoluminescence decay lifetime (τ_{em}) determines the down-conversion efficiency of the nitrogen-functionalized graphene quantum dots. With the increase in τ_{em} at $\lambda_{em} > 500$ nm, the conversion efficiencies of the NGQDs coated-CIGS solar cells increased by 12.22%. Thus, the increase in τ_{em} at $\lambda_{em} > 500$ nm significantly increased the maximum current output and thus enhanced the solar-cell performance.

Recently, carbon-based quantum dots (QDs) and graphene QDs (GQDs) have received considerable attention due to their advantageous characteristics[1]. GQDs are attractive owing to the unique broadband-tunable photoluminescent (PL) properties, their excellent biocompatibility, high photostability, low toxicity, low cost, and due to the abundance of the raw materials used to create them[2,3]. They have promising applications in bioimaging[2,4], biosensing[5,6], environmental monitoring[7], light-emitting diodes[8], and photovoltaic (PV) devices[9,10].

Previously, several research groups used GQDs as photon downconverters in silicon-based PV devices[9,10]. A downconverter absorbs photons of at short wavelengths (λ) and emits photons at longer λ levels. The downconversion efficiency (η_{dc}) of a downconverter can be determined by Eq. (1),

$$\eta_{dc} = N_{phe}/N_{pha} \tag{1}$$

where N$_{phe}$ denotes the number of useful emitted photons which can be absorbed by PV materials to generate current, and N$_{pha}$ is the total number of absorbed photons by downconverters.

[1]Center of Research Excellence in Renewable Energy (CoRERE), King Fahd University of Petroleum and Minerals (KFUPM), Dhahran, 31261, Saudi Arabia. [2]Smart Textile Convergence Research Group, Daegu Gyeongbuk Institute of Science & Technology (DGIST), 333 Techno Jungang-Daero, Hyeonpung-Myeon, Dalseong-Gun, Daegu, 42988, Republic of Korea. Correspondence and requests for materials should be addressed to J.H.K. (email: jaehyun@dgist.ac.kr)

The value of η_{dc} is essentially governed by the PL quantum yield (QY) and the Stokes shift ($\Delta\lambda$). For application in PV devices, GQDs should exhibit a high PL QY in conjunction with a large $\Delta\lambda$ value. Unfortunately, most of the reported GQDs are not suitable for application in prominent thin-film-based Cu(In, Ga)Se$_2$ (CIGS) PV cells[1,3,9–12].

On the other hand, commercial interest is beginning to shift toward thin-film cells owing to their low material and manufacturing costs[13]. However, there is still a large difference between the experimentally achieved and theoretical efficiency ($\sim$33%, $E_g \approx 1.15\,eV$)[14]. The parasitic absorption losses in the ZnO and CdS layers weaken the short-λ response, representing the predominant hurdles in the quest to realize high-performance CIGS solar cells[14–17]. The poor short-λ response is inherently linked to the interaction of short-λ photons with the front layers of solar cells. A luminescent downconverter (LDC) can be used to improve the short-λ response. For down-conversion, several LDC materials have been investigated, including GQDs[1,3,9–11], inorganic QDs[18–21], organic dyes[22,23], and rare-earth ions/complexes[24–26]. However, these are not convenient downconverters owing to one or more limitations, e.g., a low PL QY, a narrow absorption band, a small value of $\Delta\lambda$, low absorption coefficients, low stability, and toxicity. In addition, these materials are generally expensive[27]. Therefore, we previously investigated a novel approach by which to produce N-functionalized GQDs (NGQDs) rapidly. The produced NGQDs exhibited an ultrahigh PL QY and a large $\Delta\lambda$, which are mandatory for enhancing the performance capabilities of CIGS solar cells. Furthermore, the produced NGQDs was used to coat a layer onto the top of a CIGS solar cell, and the ensuing performance enhancement was studied[28].

In the present study, we tuned the synthesis parameters of NGQDs to achieve an ultrahigh PL QY along with a very large value of $\Delta\lambda$ (PL emission peak at $\lambda_{em} > 500\,nm$) via tailoring the fractions and concentrations of the N and O moieties. A new parameter — the emission-wavelength-dependent PL decay lifetime (τ_{em}) — was introduced, which greatly affects the down-conversion efficiency of NGQDs in CIGS solar cells. NGQDs with various τ_{em} values were applied to CIGS solar cells to evaluate their downconversion performance. The PL decay spectra at various emission wavelengths were recorded and used to determine the value of τ_{em}. To the best of our knowledge, the relationship between the emission-wavelength-dependent PL decay lifetime and the CIGS solar-cell performance was established for the first time [10].

Results

Various NGQDs were synthesized by controlling the polyethyleneimine (PEI)/graphene oxide (GO) weight ratio, synthesis temperature, and synthesis time. The synthesis parameters of the NGQD samples and the PL QYs are presented in Table S1. Only four samples (#3, #9, #11, and #12) exhibited a PL QY of >75%; therefore, we used these samples for a more detailed study. The other NGQDs for which PL QY < 75% do not have much of an impact on enhancing the performance of CIGS solar cells. Therefore, a detailed study of NQGDs for which the PL QY < 75% was not done.

High-resolution transmission electron microscopy (HRTEM) images of the NGQDs (#3, #9, #11, and #12) are shown in Fig. 1(a–d). These images show lattice fringes for all samples, indicating high crystallinity of the synthesized NGQDs. The spacings between the fringes were determined to be 0.346 and 0.214 nm, corresponding to the (002) and (100) planes of graphite. However, the calculated d-spacings between the basal planes of the NGQDs are slightly wider than those of graphite ($d_{002} = 0.334\,nm$ and $d_{100} = 0.213\,nm$) owing to the presence of functional groups[12]. The spacing of 0.246 nm corresponds to the lattice constant of graphite ($a = 0.246\,nm$). Figure S1 shows the size distribution of the NGQD samples. The maximum fractions of the NGQD size obtained for samples #3, #9, #11 and #12 are 3.0 nm, 2.1 nm, 1.8 nm, and 3.9 nm, respectively. The Raman spectra of the NGQDs are shown in Fig. 1(e). The peaks at 1,346 and 1,587 cm^{-1} are assigned to the characteristic D and G bands, respectively[10,11]. Thus, the spectroscopic analysis confirms the formation of NGQDs. The Fourier transform infrared (FTIR) spectra of the NGQD samples are shown in Fig. 1(f). The peaks at 3,420 and 3,215 cm^{-1} are attributed to the stretching vibrations of O–H and N–H, respectively[3]. The bond signatures of sp^2 C–H (C=C–H) at 3,005 cm^{-1}, sp^3 C–H (C–C–H) at 2,911 and 2,844 cm^{-1}, and C=O at 1,730 cm^{-1} are observed for samples #9, #11 and #12[1,3,29]. The absorption peaks due to the bond signatures of C=C at 1,666 cm^{-1} and C–H at 1,028 and 944 cm^{-1} are also observed for all of the samples[30]. The peaks at 1,028 cm^{-1} (C–H in-plane bending vibration) and 944 cm^{-1} (H out-of-plane wagging) are attributed to aromatic moieties[30]. The several peaks found in the region of 1,500–1,100 cm^{-1} are assigned to the C=C and C–N stretching modes[31,32].

The ultraviolet-visible (UV-Vis) absorption spectra of the NGQD solutions were measured in the λ range of 200–600 nm. Broad absorption was obtained all four samples above (Fig. 2(a)). The strong absorption at $\lambda < 500\,nm$ is attributed to the encompassment of several characteristic absorption bands. Typically, the $\pi \rightarrow \pi*$ transitions of C=C bonds cause absorption in the deep UV region[33,34]. However, the absorption in the low λ range (270–420 nm) corresponds to the $C\pi \rightarrow N\pi*/C\pi \rightarrow O\pi*$ transitions of C–N/C=N and C=O[35]. N doping introduces a new energy level (N$\pi*$), which is responsible for the aforementioned new peaks. In addition, the absorption peaks due to the $C\pi \rightarrow O\pi*$ transition shift toward higher wavelengths with N doping[36]. Thus, the NGQDs exhibit strong absorption for $\lambda < 500\,nm$, indicating that the produced NGQDs are extremely applicable for CIGS-based solar cells. Moreover, the absorption spectra of NGQDs synthesized with PEI/GO weight ratios of 10%, 20%, and 50% at 200–350 °C are shown in Fig. S2(a–c). The samples prepared with ratios of 10% and 20% at 350 °C exhibit weak absorption. The absorption spectra of the samples synthesized with a ratio of 20% at 300 °C for 15, 30, and 90 min are presented in Fig. S2(d).

Figure 2(b) presents the PL emission spectra recorded with $\lambda_{ex} = 405\,nm$. The PL emission range for NGQD samples #9, #11, and #12 is 460–650 nm (peak at $\sim$500 nm); however, the emission range for sample #3 is 550–650 nm (peak at $\sim$560 nm). It can be seen from Fig. 2(c) that the synthesized NGQD samples #3, #9, #11, and #12 exhibit PL QYs of 78%, 99%, 80%, and 77%, respectively. The $\Delta\lambda$ values for samples #9, #11, and #12 are identical ($\sim$95 nm); however, the value for #3 is $\sim$155 nm. The full width at half-maximum (FWHM) values for samples #3, #9, #11, and #12 are 31, 66, 66, and 66 nm, respectively. Notably, the calculated FWHM values are lower than
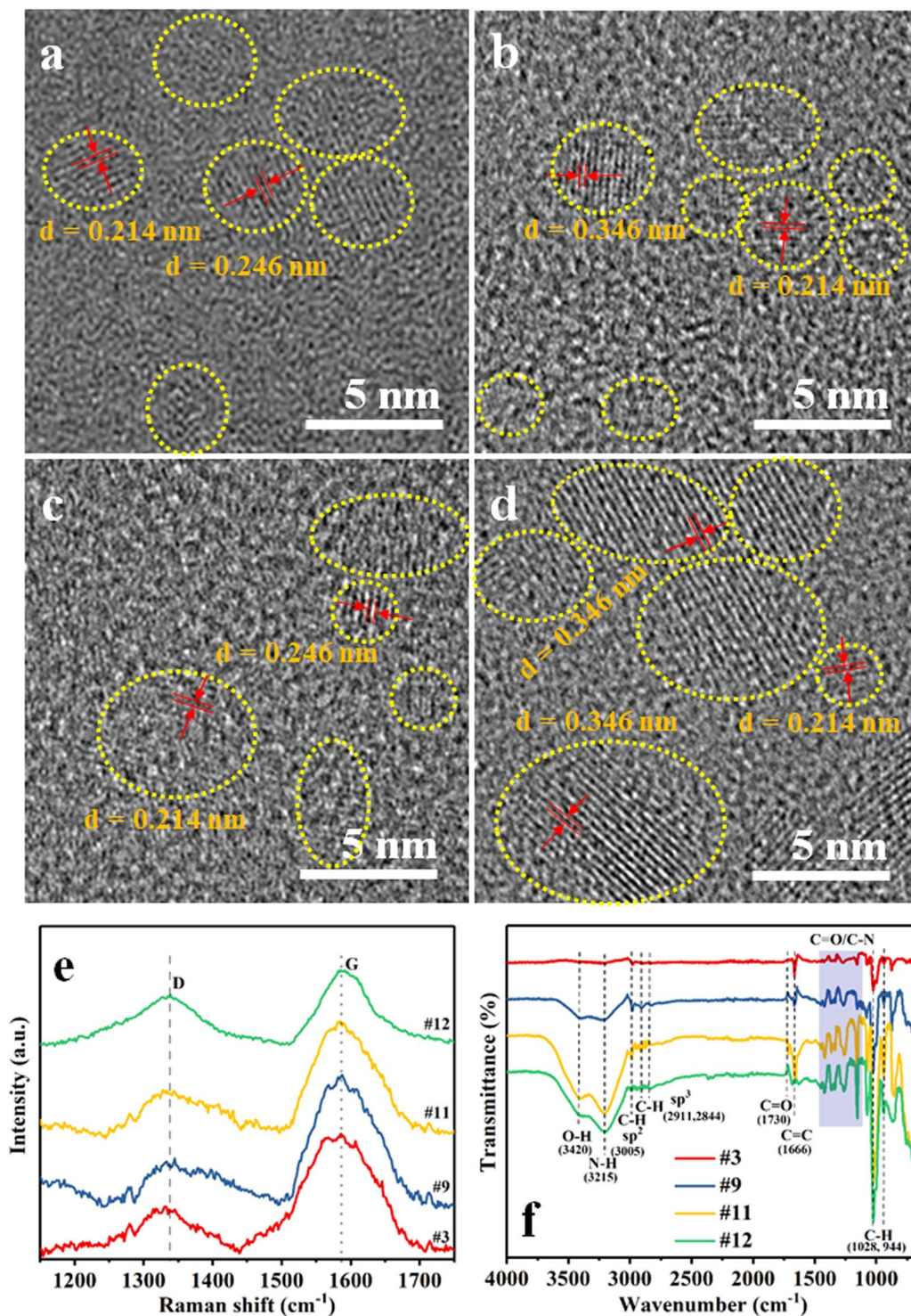
Figure 1. HRTEM images of NGQD samples (**a**) #3, (**b**) #9, (**c**) #11, and (**d**) #12. (**e**) Raman spectra and (**f**) FTIR transmittance spectra of the samples.

those reported by Qu et al.[3] Moreover, PL emission peaks at $\lambda_{ex} = 379$ nm were observed at emission wavelengths of 524 nm, 442 nm, 457 nm, and 458 nm for NGQD samples #3, #9, #11 and #12, respectively (Fig. S3). It can be noted that the PL peak positions of NGQDs at $\lambda_{ex} = 379$ nm are quite different at $\lambda_{ex} = 405$ nm. The similar, dependency of the PL peak position of NQGD on λ_{ex} is observed by several research groups[37–39]. It has been observed that the dependency of PL peak position of NQGD on λ_{ex} is due to the size of NGQDs (quantum confinement effect)[37], trap states at the surface of NGQDs (functional groups/dangling bonds)[38] and electronegativity of heteroatoms[39]. However, the proposed reasons for λ_{ex}-dependent PL position is still controversial, it needs further discussion[40].
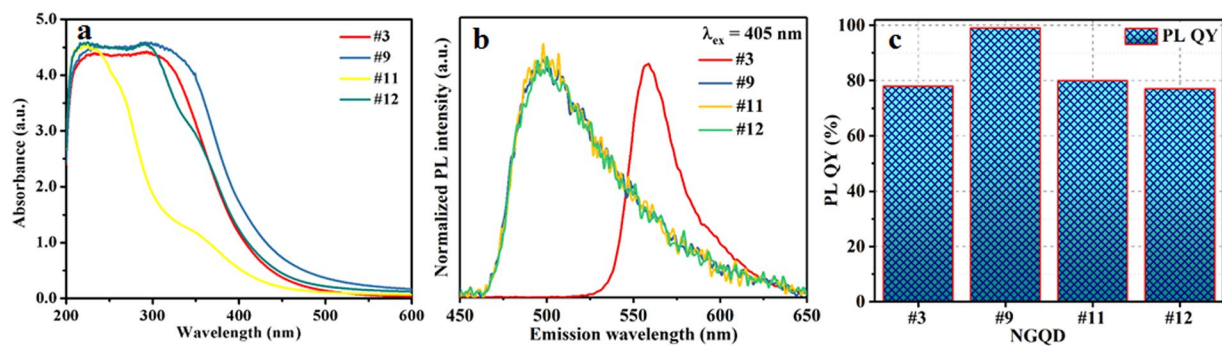
Figure 2. (**a**) UV absorbance spectra, (**b**) PL spectra emission spectra at $\lambda_{ex} = 405$ nm, and (**c**) PL QY of NGQD samples #3, #9, #11, and #12.
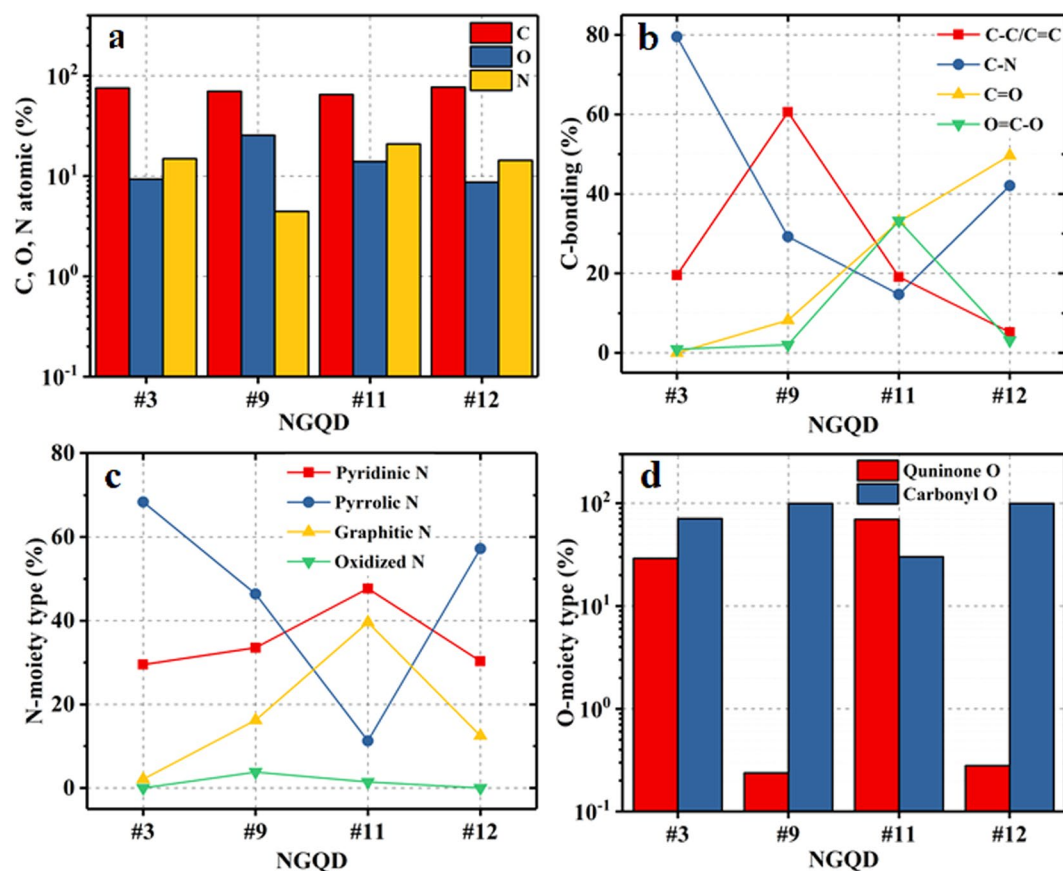

Figure 3. XPS analysis results: (**a**) atomic percentages of C, O, and N and proportions of (**b**) C-containing bonds, (**c**) N-moiety types, and (**d**) O-moiety types in NGQD samples #3, #9, #11, and #12.

We compared the absorption and the PL results between the NGQDs prepared in this study and those reported previously. These results are presented in Table S2. It can be seen that previously reported NGQDs have one or more flaws, specifically, low PL QYs, inappropriate absorption, and emission ranges, and low $\Delta\lambda$ value. Thus, previously reported NQGDs are not applicable for use in CIGS solar cells[1,3,11]. In this study, the NGQDs are highly functionalized, and hence the PL QY, absorption, and emission bands are highly dependent on N, O moieties and C bonding (Fig. 3). With the increase in the size of NGQDs, the PL QYs was decreased from >75% to ~20%, which are not applicable for CIGS solar cells. Thus, investigation of the dependency of CIGS solar cell performance on NGQDs size is not studied.

X-ray photoelectron spectroscopy (XPS) measurements were taken to study the C-containing bonds and to determine the N moieties, O moieties, and elemental compositions. The XPS elemental survey spectra (Fig. S4) exhibit three predominant peaks attributed to C1s (~284 eV), N1s (~399 eV), and O1s (~531 eV). The atomic percentages of C, O, and N are shown in Fig. 3(a). The deconvoluted C1s spectrum exhibits four peaks conforming to
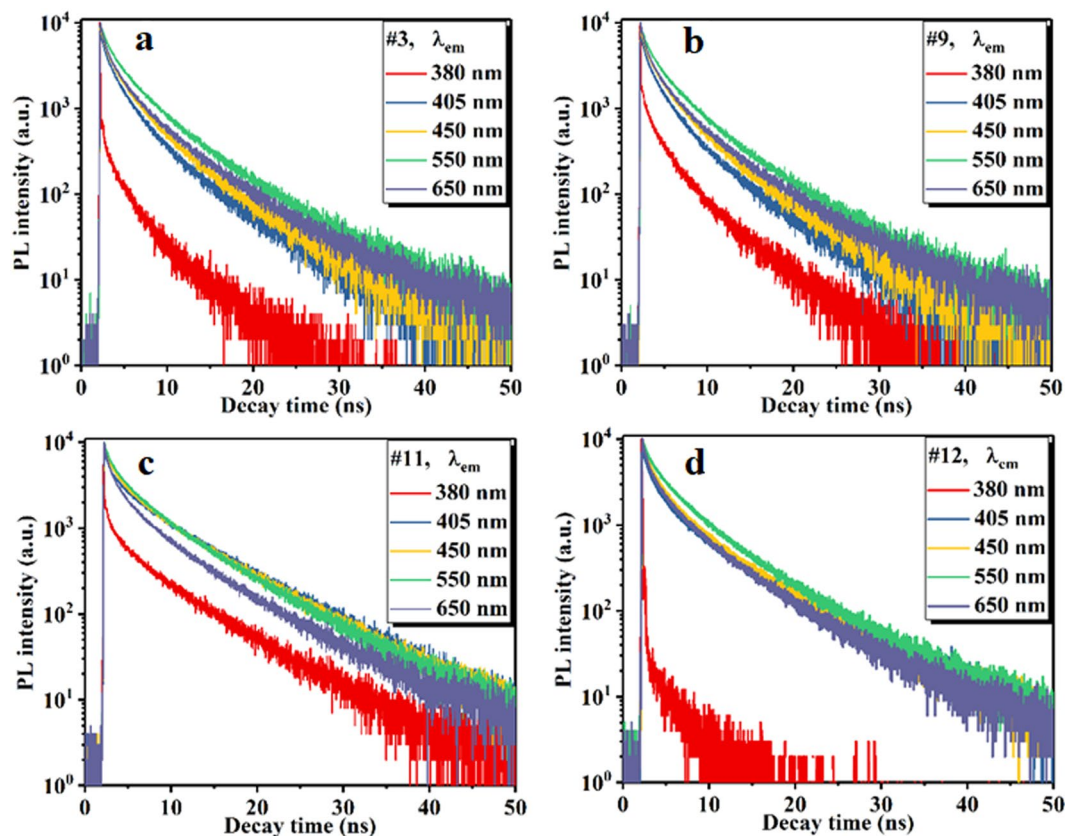
Figure 4. PL decay spectra at various emission wavelengths for NGQD samples (**a**) #3, (**b**) #9, (**c**) #11, and (**d**) #12.

C–C/C=C, C–N, C=O, and O=C–O bonds (Fig. S5)[25], and the relative proportions of these bonds in the samples are presented in Fig. 3(b). Sample #3 exhibits the largest fraction of C–N bonds (~80%); however, the proportions of C=O and O=C–O bonds are negligible in this sample. Sample #12 shows the largest fraction of C=O bonds and sample #9 shows the largest fraction of C–C/C=C bonds (~60%). The deconvoluted N1s spectrum shows four peaks which can be assigned to pyridinic, pyrrolic, graphitic, and oxidized N (Fig. S6)[26]. The proportions of the various types of N moieties in the NGQD samples are presented in Fig. 3(c). The deconvoluted O1s spectrum exhibits two peaks corresponding to quinone and carbonyl O (Fig. S7). Figure 3(d) shows that the fraction of quinone O in samples #9 and #12 is negligible[24].

Discussion

The large fractions of C-N bonding and pyridinic N may cause the largest $\Delta\lambda$ of sample #3. However, the largest fraction of C-C/C=C bonding may be responsible for the ultra-high PL QY (sample #9). The time-resolved PL decay spectra were recorded using a time-correlated single-photon counting technique at various emission wavelengths of 380, 405, 450, 550, and 650 nm for NGQDs #3, #9, #11, and #12 (Fig. 4(a–d)). The average value of τ_{em} at a given λ_{em} was determined via integration of the PL decay curve using equation (S1 of the Supplementary Information). The values of the integrated area and the calculated τ_{em} values are listed in Table S3.

A schematic of the energy levels and the possible electron transitions responsible for the photon emission is presented in Fig. 5(a). When the NGQDs are illuminated by a light source, e.g., $\lambda_{ex} = 379$ nm, the photons are absorbed, resulting in the electron transitions of C$\pi \rightarrow$ Cπ^*, C$\pi \rightarrow$ Nπ^*, or C$\pi \rightarrow$ Oπ^*. The excited electrons are deactivated via two mechanisms. One is by direct recombination after vibration relaxation due to the transition between the same energy levels, leading to PL. In this case, the PL QY can be high, but $\Delta\lambda$ is low. The other mechanism is a transition through intersystem crossing (C$\pi^* \rightarrow$ Nπ^*, C$\pi^* \rightarrow$ Oπ^*), followed by vibration relaxation[36]. Finally, the recombination occurs and produces PL. Due to the large $\Delta\lambda$, the second process is very effective for downconversion (larger values of η_{dc}).

The average values of τ_{em} were normalized with respect to the value at 550 nm (Fig. 5b). For samples #3, #9, and #12, the values of τ_{em} are larger at $\lambda_{em} = 550$ nm than at lower emission wavelengths (380, 405, and 450 nm). However, for sample #11, τ_{em} at the emission wavelength of 550 nm is smaller than those at 405 and 450 nm, indicating that the amount of emitted photons at $\lambda_{em} < 550$ nm is greater than that at $\lambda_{em} = 550$ nm. Thus, sample #11 cannot be used for downconversion in CIGS solar cells. The fraction of quinone O higher than that of carbonyl O may be the cause of the higher value of τ_{em} at the lower λ_{em} ($\lambda_{em} < 550$ nm) for sample #11. At $\lambda_{em} = 380$ nm, sample #12 exhibits the smallest τ_{em} (~38% of τ_{em} at 550 nm), while sample #11 exhibits the largest τ_{em} (~96%
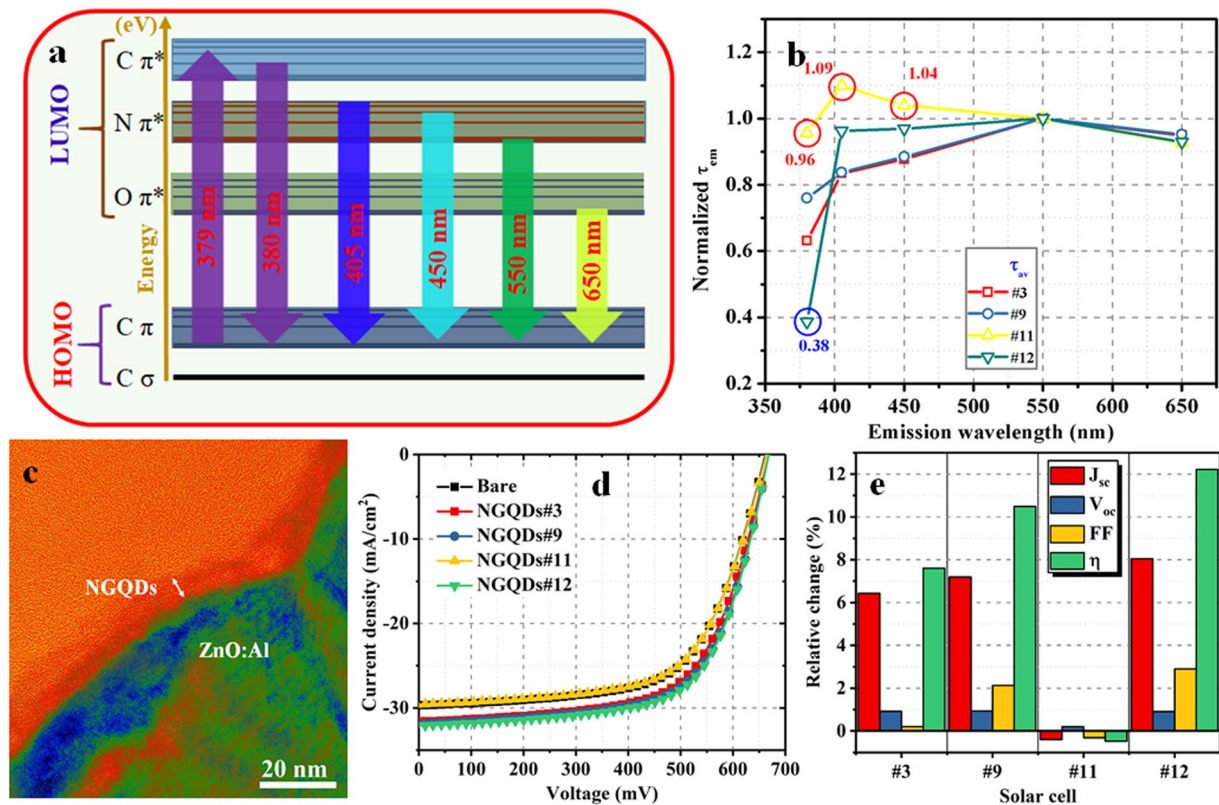
Figure 5. (**a**) Schematic of possible transitions at various emission wavelengths. (**b**) Normalized τ_{em} values of NGQD samples #3, #9, #11, and #12. (**c**) Cross-sectional HRTEM image of the ZnO:Al/NGQD interface. (**d**) $J–V$ characteristics of NGQD-CIGS solar cells #3, #9, #11, and #12. (**e**) Relative change in the performance parameters of CIGS solar cells.

of τ_{em} at 550 nm). These findings indicate that the ratios of the number of photons emitted at $\lambda_{em} = 380$ nm to the number of photons emitted at $\lambda_{em} = 550$ nm are correspondingly 0.38 and 0.96 for samples #11 and #12. The emitted photons at a wavelength of 380 nm make no contribution to the generation of current. Therefore, the maximum loss arises for sample #11, whereas this loss is minimum for sample #12 (Fig. 5b). The value of τ_{em} for NGQDs at a particular emission wavelength indicates the effectiveness of the photon emission at that wavelength. To the best of our knowledge, this is the first report of PL-decay-lifetime-dependent photon emission efficiency and its impact on solar energy conversion. In addition to the $\Delta\lambda$ and PL QY values, the decay lifetimes at slow transitions play a significant role in determining the conversion efficiency (η) of solar cells. At a particular wavelength, a larger τ_{em} indicates more effective photon emission. An NGQD layer with a thickness of ~4 nm was realized on the front surface of the cell (Fig. 5c). Current density–voltage ($J–V$) characterization was carried out under illuminated to evaluate the performance capability of the cells (Fig. 5d). The performance parameters (short-circuit current density J_{sc}, open-circuit voltage V_{oc}, fill factor FF, and η) were extracted from the experimentally obtained $J-V$ curves. The values of η and FF were determined using Eqs S2 and S3, respectively (see Supplementary Information).

The J_{sc} values obtained for the bare (reference) solar cell and for NGQD-coated CIGS (NGQD-CIGS) solar cells #3, #9, #11, and #12 were 29.71 and 31.61, 31.85, 29.59, and 32.09 mA/cm^2, respectively. The relative change in the performance parameters is presented in Fig. 5(e). The relative changes in J_{sc} for NGQD-CIGS solar cells #3, #9, #11, and #12 was 6.4%, 7.19%, −0.41%, and 8.04%, respectively. The observed enhancement in J_{sc} for NGQD-CIGS solar cells #3, #9, and #12 is attributed to photon downconversion and light trapping. However, the J_{sc} value was slightly reduced for NGQD-CIGS solar cell #11. Further, a slight change in V_{oc} was observed for NGQD-CIGS solar cells #3, #9, #11, and #12 (relative changes: 0.92%, 0.93%, −0.09%, and 0.91%, respectively). NGQD-CIGS solar cells #3, #9, and #12 showed a slight improvement in the FF value. The overall enhancements in η for NGQD-CIGS solar cells #3, #9, and #12 were 7.60%, 10.49%, and 12.22%, respectively; however, a slight reduction in η was observed for NGQD-CIGS solar cell #11. Thus, the η_{dc} of NGQDs is mainly determined by the decay lifetimes at various λ_{em} values.

When any fluorescent material is excited with light with energy exceeding the corresponding band-gap, the light is absorbed and the electron moves to an excited state (a higher energy level). The excited electron attempts to return into its original position (initial energy level) by losing energy in the form of heat or light. Two main transitions involved in this process. First, the transition without light emission is called non-radiative recombination (fast band-to-band transition). Second, radiative recombinations occur during which light is emitted (due to slow extrinsic-effect-induced transitions)[40,41]. The usefulness of the emitted light can be determined by the average
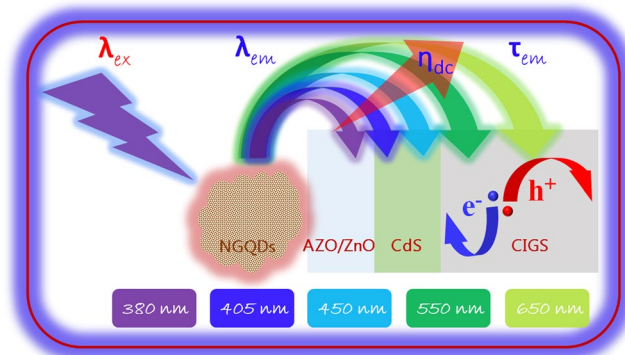
Figure 6. Schematic of the emission wavelength (λ_{em})-dependent PL decay lifetime (τ_{em}) at $\lambda_{em} = 379$ nm, for the utilization of photons as charge carriers in NGQD-CIGS solar cells.
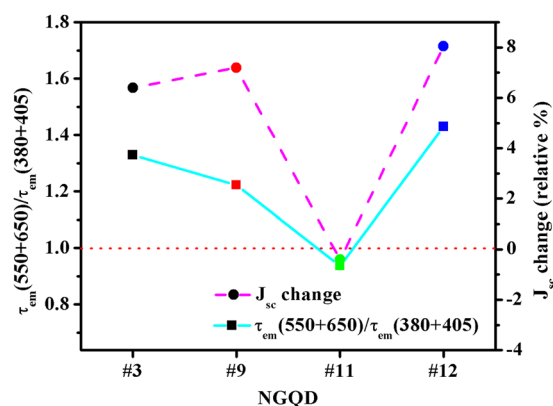

Figure 7. Ratio of the sum of τ_{em} values at higher λ_{em} (550 and 650 nm) to sum of τ_{em} values at lower λ_{em} (380 and 405 nm) NGQD samples and corresponding obtained J_{sc} values for NGQD-CIGS solar cells.

value, τ_{em}. The energy-dependence lifetime of the emitted photons and their utilization as charge carriers in the NGQD-CIGS solar cells at $\lambda_{ex} = 379$ nm are shown in Fig. 6. The η_{dc} value is replicated in the obtained J_{sc} change (ΔJ_{sc}). It can be seen that emitted light of various wavelengths can be absorbed in the different part of the CIGS solar cells. Light for which $\lambda_{em} > 500$ nm can easily be absorbed in the CIGS absorber, with most of these photons used for the current generation. However, a large fraction of the light for which $\lambda_{em} < 500$ nm absorbed in the ZnO/CdS layers is not used for the current generation. Therefore, the fraction of emitted light should be higher for cases in which $\lambda_{em} > 500$ nm to enhance the performance of the CIGS cells. Accordingly, τ_{em} should be higher for $\lambda_{em} > 500$ nm. Hence, for better utilization of the emitted photons in NGQD-CIGS solar cells, the values of τ_{em} for $\lambda_{em} < 500$ nm should be lower and the values of τ_{em} for $\lambda_{em} > 500$ nm should be higher. Photons for which $\lambda_{em} \approx 450$ nm partially contribute to the generation of current. Therefore, the ratio (R_{em}) of the sum of the τ_{em} values at higher values of λ_{em} (550 and 650 nm, $\tau_{em} > 500$ nm) to the sum of τ_{em} values at lower values of λ_{em} (380 and 405 nm, $\tau_{em} < 500$ nm) NGQD samples along with the corresponding obtained ΔJ_{sc} values for NGQD-CIGS solar cells are shown in Fig. 7. A trend similar to that of the variations of R_{em} and ΔJ_{sc} was obtained. No change in J_{sc} ($\Delta J_{sc} = 0$) was observed when $R_{em} = 1$ (as shown by the red dotted horizontal line). For cases in which $R_{em} > 1$, an enhancement in J_{sc} was obtained. However, J_{sc} was reduced slightly when $R_{em} < 1$ (NGQD-CIGS #11).

NGQDs with ultrahigh PL QYs (along with large $\Delta\lambda$ values) was achieved by tuning the N and O moieties through control of the N-dopant concentration, synthesis temperature, and synthesis duration.

In this work, the important parameters influencing the down-conversion efficiency of the NGQDs are highlighted. In addition to the ultrahigh QY and large Stokes shift, the emission-wavelength-dependent PL decay lifetime plays a significant role in enhancing the down-conversion efficiency. The measured PL QYs of NGQD samples #3, #9, #11, and #12 were 78%, 99%, 80%, and 77%, respectively, and the corresponding calculated Stokes shifts were ~155, ~95, ~95, and ~95 nm. The observed enhancements in η for solar cells with NGQD samples #3, #9, and #12 were 7.60%, 10.49%, and 12.22%, respectively; however, NGQD-CIGS solar cell #11 exhibited a slightly lower η enhancement. NGQD-CIGS solar cell #12 exhibited the smallest τ_{em} at $\lambda_{em} = 380$ nm. By increasing the PL decay lifetime at $\lambda_{em} > 500$ nm, the CIGS solar-cell performance can be enhanced. This synthesis technology is economical and environmentally friendly. These low-cost processed NGQDs can be used to enhance the performance of the CIGS solar cells. The results of this study reveal that downconverters should have extremely low PL decay lifetime values at $\lambda_{em} < 500$ nm and high values at $\lambda_{em} > 500$ nm before they can be appropriately applied to CIGS solar cells.

Materials and Methods

Synthesis of NGQDs. First, an aqueous solution of GO ($4.0\,\mathrm{mg\,mL^{-1}}$) was prepared by mixing GO powder in deionized (DI) water. An aqueous solution of PEI ($0.5\,\mathrm{g\,mL^{-1}}$) was used as the N source. For the synthesis of NGQDs, PEI/GO solution mixtures were prepared with PEI/GO weight ratios of 10%, 20%, and 50% (denoted as PEI10, PEI20, and PEI50, respectively). Subsequently, GO was functionalized by stirring the PEI/GO solution mixture at 90 °C. Next, we synthesized NGQDs via heat treatment of the PEI/GO composites at various temperatures in an N_2 environment for different durations. The products were then dispersed in ethanol and the solutions were filtered. The methodology used for the PL QY calculation is described in the Supplementary Information.

Characterization of NGQDs. The absorbance spectra of the NGQDs were recorded using a UV–vis–near-infrared spectrophotometer (Carry-5000, Agilent Technologies). The PL spectra were recorded at excitation wavelengths (λ_{ex}) of 379 and 405 nm using a PL spectrophotometer (Darsa, PSI Trading Co. Ltd.) with a Xe lamp. Time-resolved PL decay was measured via the time-correlated single-photon counting (TCSPC) technique using a time-resolved spectroscopy system (TRSS, Fluo Time 200, PicoQuant). A laser with an excitation wavelength of 379 nm was used to excite all of the NGQD samples. A photomultiplier tube (PMT) was used for the detection of the emitted light by the NGQD samples. To study the atomic structure of the NGQDs, HRTEM (HF-3300/NB5000/S-4800, Hitachi) was utilized. The elemental composition of the NGQDs was determined via XPS (ESCALAB 250Xi, Thermo Fisher Scientific). The XPS peaks were calibrated using the C1s peak. The Raman spectra were recorded using a confocal Raman spectrometer (Nicolet Almega XR, Thermo Fisher Scientific) with a λ_{ex} value of 532 nm.

Solar-cell fabrication and characterization. The details of the CIGS solar-cell fabrication process are presented in the Supplementary Information. CIGS solar cells were initially fabricated, after which the synthesized NGQDs were coated onto the top of the solar cells. The J–V characteristics (active area of ~0.43 cm^2) were measured under 1-sun AM1.5 G illumination using a source meter (Keithley 2400). The illumination intensity was calibrated using a Si reference solar cell (PV Measurements, USA). All measurements were performed at 25 °C.

References

1. Que, D. *et al.* Formation mechanism and optimization of highly luminescent N-doped graphene quantum dots. *Sci. Rep.* **4**, 5294-1–5294-9 (2014).
2. Sun, H., Wu, L., Gao, N., Ren, R. & Qu, X. Improvement of photoluminescence of graphene quantum dots with a biocompatible photochemical reduction pathway and its bioimaging application. *ACS Appl. Mater. Interfaces* **5**, 1174–1179 (2013).
3. Qu, D., Zheng, M., Xie, Z. & Sun, Z. Tailoring color emissions from N-doped graphene quantum dots for bioimaging applications. *Light: Sci. Appl.* **4**, e364-1–e364-8 (2015).
4. Pan, D. *et al.* Cutting sp^2 clusters in graphene sheets into colloidal graphene quantum dots with strong green fluorescence. *J. Mater. Chem.* **22**, 3314–3318 (2012).
5. Zhao, H. *et al.* A universal immunosensing strategy based on regulation of the interaction between graphene and graphene quantum dots. *Chem. Commun.* **49**, 234–236 (2013).
6. Fan, Z., Li, S., Yuan, F. & Fan, L. Fluorescent graphene quantum dots for biosensing and bioimaging. *RSC Adv.* **5**, 19773–19789 (2015).
7. Bai, J. M., Zhang, L., Liang, R. P. & Qiu, J. D. Graphene quantum dots combined with europium ions as photoluminescent probes for phosphate sensing. *Chem. Eur. J.* **19**, 3822–3826 (2013).
8. Dong, P. *et al.* Synthesis of white-light-emitting graphene quantum dots via a one-step reduction and their interfacial characteristics-dependent luminescence properties. *Inorg. Chem. Front.* **4**, 712–718 (2017).
9. Lee, K. D. *et al.* Graphene quantum dot layers with energy-down-shift effect on crystalline-silicon solar cells. *ACS Appl. Mater. Interfaces* **7**, 19043–19049 (2015).
10. Tsai, M. L. *et al.* Efficiency enhancement of silicon heterojunction solar cells via photon management using graphene quantum dots as downconverters. *Nano Lett.* **16**, 309–313 (2016).
11. Sun, J. *et al.* Ultra-high quantum yield of graphene quantum dots: aromatic-nitrogen doping and photoluminescence mechanism. *Part. Part. Syst. Charact.* **32**, 434–440 (2015).
12. Tang, L. *et al.* Deep ultraviolet to near-infrared emission and photoresponse in layered N-doped graphene quantum dots. *ACS Nano* **8**, 6312–6320 (2014).
13. Graham-Rowe, D. Solar cells get flexible. *Nat. Photon.* **1**, 433–435 (2007).
14. Siebentritt, S. What limits the efficiency of chalcopyrite solar cells? *Sol. Energy Mater. Sol. Cells* **95**, 1471–1476 (2011).
15. Klenk, R. & Lux-Steiner, M. C. In Thin Film Solar Cells Fabrication, Characterization and Applications (eds Poortsmans, J. & Arkhipov, V.) Ch. 6 (John Wiley 0026 Sons, Ltd, 2006).
16. Klampaftis, E., Ross, D., McIntosh, K. R. & Richards, B. S. Enhancing the performance of solar cells via luminescent down-shifting of the incident spectrum: a review. *Sol. Energy Mater. Sol. Cells* **93**, 1182–1194 (2009).
17. Shafarman, W. N., Siebentritt, S. & Stolt, L. In Handbook of Photovoltaic Science and Engineering 2nd ed. (eds Luque, A. & Hegedus, S.) Ch. 13 (John Wiley & Sons, Ltd, 2011).
18. Svrcek, V., Slaoui, A. & Muller, J. C. Silicon nanocrystals as light converter for solar cells. *Thin Solid Films* **451–452**, 384–388 (2004).
19. Muffler, H. J. *et al.* Colloid attachment by ILGAR-layers: creating fluorescing layers to increase quantum efficiency of solar cells. *Sol. Energy Mater. Sol. Cells* **90**, 3143–3150 (2006).
20. van Sark, W. G. J. H. M. Enhancement of solar cell performance by employing planar spectral converters. *Appl. Phys. Lett.* **87**, 151117-1–151117-3 (2005).
21. van Sark, W. G. J. H. M., Meijerink, A., Schropp, R. E. I., van Roosmalen, J. A. M. & Lysen, E. H. Enhancing solar cell efficiency by using spectral converters. *Sol. Energy Mater. Sol. Cells* **87**, 395–409 (2005).
22. Maruyama, T., Enomoto, A. & Shirasawa, K. Solar cell module colored with fluorescent plate. *Sol. Energy Mater. Sol. Cells* **64**, 269–278 (2000).
23. Richards, B. S. & McIntosh, K. R. Overcoming the poor short wavelength spectral response of CdS/CdTe photovoltaic modules via luminescence down-shifting: ray-tracing simulations. *Prog. Photovolt.* **15**, 27–34 (2007).
24. Marchionna, S. *et al.* Photovoltaic quantum efficiency enhancement by light harvesting of organo-lanthanide complexes. *J. Lumin.* **118**, 325–329 (2006).
25. Kawano, K., Hashimoto, N. & Nakata, R. Effects on solar cell efficiency of fluorescence of rare-earth ions. *Mater. Sci. Forum* **239–241**, 311–314 (1997).

26. Kawano, K., Arai, K., Yamada, H., Hashimoto, N. & Nakata, R. Application of rare-earth complexes for photovoltaic precursors. *Sol. Energy Mater. Sol. Cells* **48**, 35–41 (1997).
27. Rowan, B. C., Wilson, L. W. & Richards, B. S. Advanced material concepts for luminescent solar concentrators. *IEEE J. Sel. Top. Quant. Electron.* **14**, 1312–1322 (2008).
28. Khan, F. & Kim, J. H. N-functionalized graphene quantum dots with ultrahigh quantum yield and large Stokes shift: efficient downconverters for CIGS solar cells. *ACS Photon.* **5**, 4637–4643 (2018).
29. Zhu, S. *et al.* Highly photoluminescent carbon dots for multicolor patterning, sensors, and bioimaging. *Angew. Chem. Int. Ed.* **52**, 3953–3957 (2013).
30. Hwang, E. *et al.* Chemically modulated graphene quantum dot for tuning the photoluminescence as novel sensory probe. *Sci. Rep.* **6**, 39448-1–39448-10 (2016).
31. Meyer, J. C. *et al.* The structure of suspended graphene sheets. *Nature* **446**, 60–63 (2007).
32. Casiraghi, C. *et al.* Rayleigh imaging of graphene and graphene layers. *Nano Lett.* **7**, 2711–2717 (2007).
33. Eda, G. *et al.* Blue photoluminescence from chemically derived graphene oxide. *Adv. Mater.* **22**, 505–509 (2010).
34. Liu, F. *et al.* Facile synthetic method for pristine graphene quantum dots and graphene oxide quantum dots: origin of blue and green luminescence. *Adv. Mater.* **25**, 3657–3662 (2013).
35. Lingam, K., Podila, R., Qian, H., Serkiz, S. & Rao, A. M. Evidence for edge-state photoluminescence in graphene quantum dots. *Adv. Funct. Mater.* **23**, 5062–5065 (2013).
36. Tang, L., Ji, R., Li, X., Teng, K. S. & Lau, S. P. Energy-level structure of nitrogen-doped graphene quantum dots. *J. Mater. Chem. C* **1**, 4908–4915 (2013).
37. Gan, Z., Wu, X., Zhou, G., Shen, J. & Chu, P. K. Is there real upconversion photoluminescence from graphene quantum dots? *Adv. Optical Mater.* **1**, 554–558 (2013).
38. Cao, L., Meziani, M. J., Sahu, S. & Sun, Y. P. Photoluminescence propertiesof graphene versus other carbon nanomaterials. *Acc. Chem. Res.* **46**, 171–180 (2013).
39. Yang, S. W. *et al.* Large-scale fabrication of heavy doped carbon quantum dots with tunable-photoluminescence and sensitive fluorescence detection. *J. Mater. Chem. A* **2**, 8660–8667 (2014).
40. Gan, Z., Xu, H. & Hao, Y. Mechanism for exciation-dependent photoluminescence from graphene quantum dots and other graphene oxide derivates: consensus, debates and challenges. *Nanoscale* **8**, 7794 (2016).
41. Kim, S. *et al.* Anomalous behaviors of visible luminescence from graphene quantum dots: interplay between size and shape. *ACS Nano.* **6**, 8203–8208 (2012).

Acknowledgements

Author Contributions

Both the authors conceived the concept and designed the experiments; F.K. performed the experiments; J.H.K. analyzed the results. F.K. wrote the paper. Both the authors reviewed the manuscript.

Additional Information

Competing Interests: The authors declare no competing interests.

Publisher's note: Springer Nature remains neutral with regard to jurisdictional claims in published maps and institutional affiliations.